JACS
JOURNAL OF THE AMERICAN CHEMICAL SOCIETY
pubs.acs.org/JACS
Article

Proton Relay for the Rate Enhancement of Electrochemical Hydrogen Reactions at Heterogeneous Interfaces

Yang Qiu, Debmalya Ray, Litao Yan, Xiaohong Li, Miao Song, Mark H. Engelhard, Junming Sun, Mal-Soon Lee, Xin Zhang, Manh-Thuong Nguyen, Vassiliki-Alexandra Glezakou, Yong Wang, Roger Rousseau,* and Yuyan Shao*

Cite This: https://doi.org/10.1021/jacs.3c06398
Read Online
ACCESS | Metrics & More | Article Recommendations | Supporting Information

ABSTRACT: Proton transfer is critically important to many electrocatalytic reactions, and directed proton delivery could open new avenues for the design of electrocatalysts. However, although this approach has been successful in molecular electrocatalysis, proton transfer has not received the same attention in heterogeneous electrocatalyst design. Here, we report that a metal oxide proton relay can be built within heterogeneous electrocatalyst architectures and improves the kinetics of electrochemical hydrogen evolution and oxidation reactions. The volcano-type relationship between activity enhancement and pK_a of amine additives confirms this improvement; we observe maximum rate enhancement when the pK_a of a proton relay matches the pH of the electrolyte solution. Density-functional-theory-based reactivity studies reveal a decreased proton transfer energy barrier with a metal oxide proton relay. These findings demonstrate the possibility of controlling the proton delivery and enhancing the reaction kinetics by tuning the chemical properties and structures at heterogeneous interfaces.

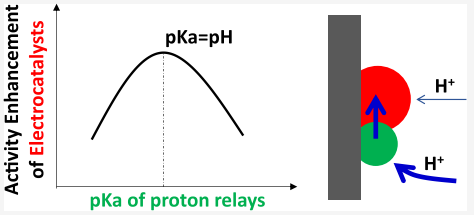

INTRODUCTION

Conventional design of heterogeneous electrocatalysts has focused on modifying the catalyst surface electronic structure through alloying,[1−3] crystalline structuring,[4] and atomic ordering and orientation[5,6] to tune the covalent interactions of surfaces with reaction intermediates (e.g., surface binding or adsorption).[7−9] These approaches have led to significant progress in improving catalyst activity for a variety of electrocatalytic reactions, including the hydrogen evolution and oxidation reaction (HER/HOR),[10,11] the oxygen evolution and reduction reaction (OER/ORR),[12,13] CO_2 reduction reactions (CO_2RR),[14,15] etc. In nature, the kinetics of these reactions are governed not only through covalent interactions but also through noncovalent interactions, the most important of which is tuning proton transfer near the catalyst surface.[16−18]

Proton transfer plays a critical role in diverse chemical, biochemical, and electrochemical processes.[19−23] The hydrogenase enzyme, microalgae, and bacteria achieve reversible proton-coupled chemical transformations by precisely controlling proton movement to and from the active sites of, for example, iron or nickel complexes with organic ligands (e.g., porphyrins or polypyridine).[24−27] To mimic the function of how natural systems manipulate proton transfer, many artificial molecular electrocatalysts have been designed and synthesized in which certain basic pendant groups function as proton relays to promote proton transfer and improve reaction kinetics.[28−31] Recently, significant improvement of ORR kinetics on Pt and Au electrocatalysts has been demonstrated through tuning proton transfer by modifying electrodes with protonic ionic liquids, while ORR reaction pathways on a heterogenized molecular Cu electrocatalyst can be controlled through a lipid-bound proton carrier.[16,19] Progress has been made in understanding the critical role of protons in the electrochemical transformation of organic molecules (formic acid,[32] alcohol,[33] nitrobenzene[34]) and hydrogen[35,36] at heterogeneous interfaces. Molecular control of heterogeneous electrocatalysis has been achieved through the graphite-conjugated acid approach.[37,38] Progress has also been made in understanding how noncovalent interactions affect heterogeneous electrocatalysis through tuning electrolyte composition.[39−41] We, therefore, hypothesize that a proton relay can be built in heterogeneous electrocatalysts to more efficiently promote proton transfer and improve electrochemical reaction kinetics for which a proton is involved in the elementary step of the specific reaction (i.e., H^+-containing reactions); Scheme 1. Heterogeneous electrocatalysts incorporating such relays would provide significant advantages over molecular electrocatalysts and organically modified electrodes, including enhanced stability and ease of deployment (in functioning devices).

Received: June 16, 2023
Revised: November 1, 2023
Accepted: November 3, 2023

Scheme 1. Hypothetical Proton Transfer with/without Metal Oxide Proton Relay

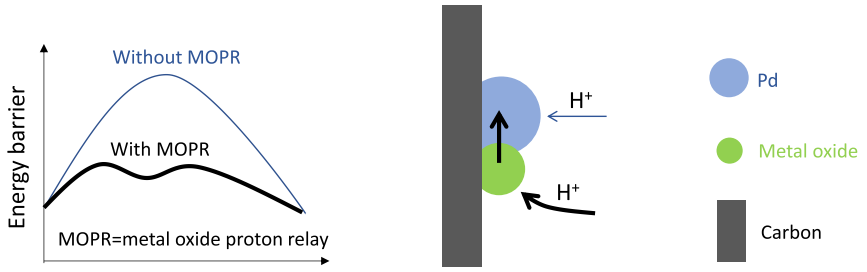

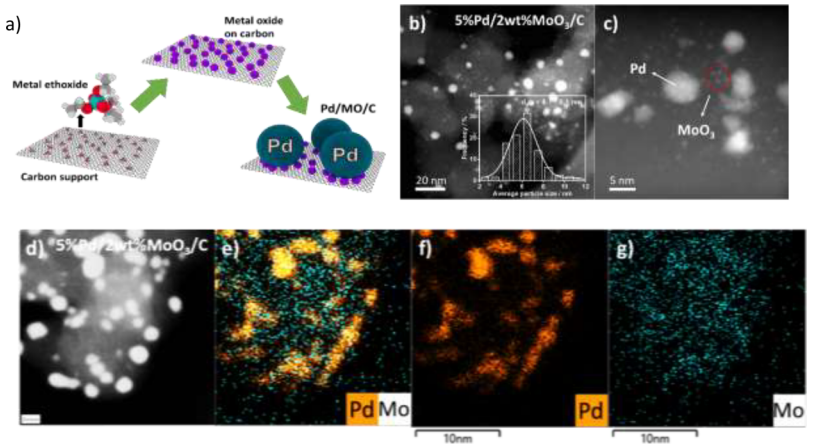

Figure 1. Synthesis and characterization of Pd/MO_x/C electrocatalysts. (a) Schematic of the Pd/MO_x/C electrocatalyst synthesis process, (b–d) STEM images of Pd/MoO_3/C, and (e–g) element mapping of Pd/MoO_3/C.

Upon searching for robust proton relay materials, we noticed that hydrated metal oxides enable proton transfer on their surface, the so-called proton hopping phenomenon.[42−45] For proton transfer from the bulk electrolyte to electrode surfaces such as metal catalyst electrodes, the hydrated metal oxide located near metal catalysts may allow (1) proton transfer on the metal oxide/water interface via the processes of hydrogen bond formation and cleavage (i.e., chain reaction) and (2) proton transfer on the metal oxide surface through Brønsted acid/base sites without the assistance of adjacent H_2O molecules, followed by proton adsorption on the metal surface. Considering that the metal oxide surface (i.e., protonation/deprotonation state) could be significantly affected by its surface acidity (i.e., pK_a) and solution pH, we postulate that the proton transfer on and from/to the metal oxide surface can be governed by its surface acidity and solution pH, thereby controlling overall reaction kinetics.

We selected MoO_3, WO_3, ZrO_2, and CeO_2 as proton relay candidates in our study because they have been well studied for their surface acidity trend (i.e., their surface pK_a(s) values range from 1.05 to 10.2),[44,46−50] and they are relatively stable in solutions of a wide range of pHs. We use HER/HOR on Pd/C catalysts as the exemplar reactions because of the well-studied HER/HOR reaction mechanisms on Pd, in which the proton-involved Volmer step is the rate-determining step (RDS). In addition, Pd is less active than Pt on which HER/HOR kinetics in acidic media can be reasonably measured using a rotating disk electrode (RDE) setup.[51−53] The maximum HER/HOR activity enhancement was obtained on Pd/MO/C (MO = metal oxide) when the metal oxide pK_a value was close to the electrolyte pH value, which strongly indicates a proton relay effect of metal oxides. Density functional theory (DFT) simulations demonstrate that (1) the lowered proton transfer energy barrier between the metal oxide surface and Pd nanoparticle opens up new channels for the Volmer reaction, which has a maximum rate when the pK_a of the metal oxide is in resonance with the solution pH; (2) the number and proximity of the MO/Pd interface sites have a significant impact on the proton transfer rate. The first property related to the rate enhancement is intrinsic to the metal oxide, and the second property is related to material architecture.

Given that more precise pK_a values across a broader range are available in the literature for amine molecules than for metal oxides, multiple amine molecules with pK_a values ranging from −2.95 to 15.2 were selected as additives to further study the relationship between HER/HOR activity improvement and pK_a (of amines) vs pH (of electrolyte solution). A volcano-type relationship of HER/HOR activity on Pd versus pK_a was observed, with the maximum activity enhancement when the amine's pK_a value matches the solution pH. These results further support the proton relay effect in this system. Our work demonstrates the first built-in, metal oxide proton relay in heterogeneous electrocatalysts, opening a new avenue for future electrocatalyst design and applications in proton-involved electrocatalytic reactions.

RESULTS AND DISCUSSION

We first deposited metal oxide (MO) nanoparticles (NPs) on a porous carbon support through the thermal decomposition of metal ethoxide precursors (Figure 1a). High-angle annular dark-field scanning transmission electron microscopy (HAADF-STEM) images show the uniform dispersion of metal oxide NPs with size between subnanometer and 1−2 nm

https://doi.org/10.1021/jacs.3c06398
J. Am. Chem. Soc. XXXX, XXX, XXX−XXX

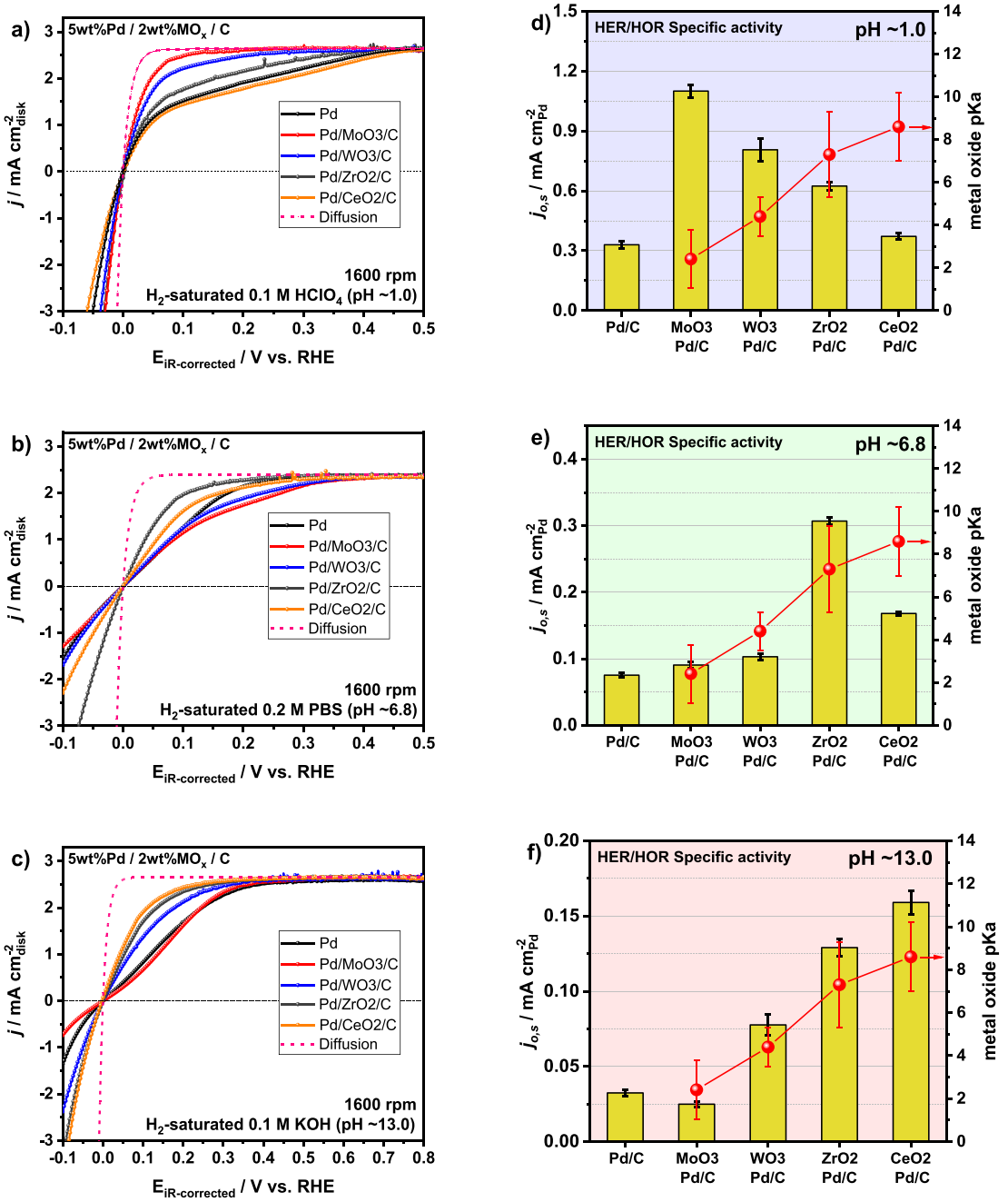

Figure 2. Kinetics measurements of HER/HOR on Pd/MO/C electrocatalysts in acidic, neutral, and alkaline electrolytes. (a−c) Linear sweep voltammetry (LSV) curves and (d−f) specific exchange current densities, pK_a value was cited as MoO_3 of 1.05−3.77;[47] WO_3 of 3.5−5.3;[46,47] ZrO_2 of 5.3−9.3;[44,50] and CeO_2 of 7−10.2.[48,49]

on carbon support (Figure S1). Pd NPs were then grown on metal oxide/carbon composites with an average size of ~6.5 nm determined by STEM for all Pd/MO/C samples (Figures 1b,c and S2), which is in good agreement with the size of ~6.4 nm calculated from X-ray powder diffraction (XRD) patterns, while no diffraction patterns of metal oxides can be observed because of their small particle size (Figure S3). HAADF-STEM and elemental mapping images reveal the close contact of Pd NPs with metal oxide NPs on the carbon surface (Figures 1d−g and S4). X-ray photoelectron spectroscopy (XPS) characterizations show two well-defined Pd $3d_{5/2}$ and $3d_{3/2}$ peaks centered at 335.4 and 340.7 eV (3), respectively (Figure S5). The positive shift of 0.2 to 0.4 eV for Pd binding energy of Pd/MO/C samples in comparison with Pd/C suggests the interaction between Pd and metal oxides, secondary evidence for the close contact between Pd and metal oxides. Diffuse reflectance infrared Fourier transform spectroscopy (DRIFTS) analysis reveals multiple Brønsted acid peaks on MoO_3, WO_3, ZrO_2, and CeO_2 surfaces when metal oxides are hydrated (Figure S6). Cumulatively, these physical characterization results confirm that the interface is formed between metal oxides and Pd NPs, and Brønsted acid sites (which are prerequisites for proton transfer from the metal oxide surface to Pd) are formed on metal oxide surfaces.

The HOR/HER polarization curves were measured using RDE in three representative electrolytes: H_2 saturated 0.1 M

https://doi.org/10.1021/jacs.3c06398
J. Am. Chem. Soc. XXXX, XXX, XXX−XXX

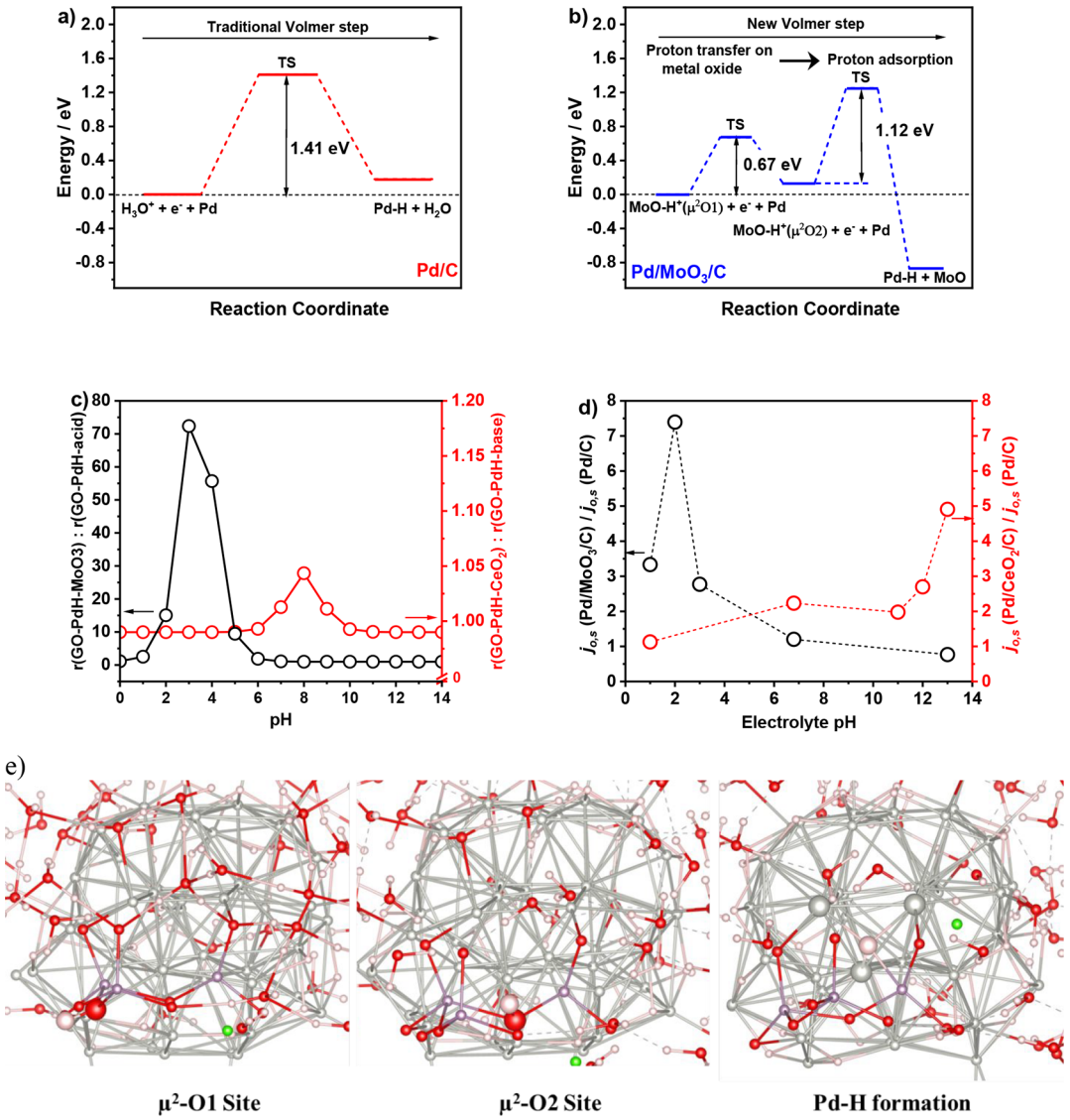

Figure 3. Proton transfer energy barrier and rate enhancement. (a, b) Computed electronic energy (eV) diagram of the Volmer reaction for (a) GO-PdH-acid and (b) GO-PdH-MoO_3 model systems, (c) computed rate enhancement factor as a function of pH for the GO-PdH-MoO_3 and GO-PdH-CeO_2 system with respect to the GO-PdH-acid and GO-PdH-base system respectively, (d) Ratio of experimental exchange current densities as a function of pH for the Pd/MoO_3/C and Pd/CeO_2/C with respect to Pd/C. (e) Snapshot showing the movement of a proton between different m^2 sites of MoO_3 and formation of a Pd−H bond. Highlighted (larger) atoms are involved in reaction mechanism. Color code: O (red), Pd (gray), Mo (light purple), H (light pink), Cl (green).

$HClO_4$ (pH 1.0), 0.2 M PBS (pH 6.8), and 0.1 M KOH (pH 13.0) (Figure 2a−c). All Pd/C and Pd/MO/C samples show reversible and similar Tafel behavior (Figure S7) for HER and HOR, indicating the reversible HER/HOR on Pd. The Tafel slopes of 81−127 mV dec^{-1} in the acidic electrolyte on Pd/C and Pd/MO/C are similar to those in neutral (92−152 mV dec^{-1}) and alkaline (98−134 mV dec^{-1}) electrolytes (Table S2). This demonstrates that the HER/HOR mechanism on Pd (with/without metal oxides) in the above three representative pH electrolytes is the same, i.e., theVolmer−Tafel mechanism with Volmer step as the RDS (Volmer step: $H^+ + e^- + * \leftrightarrow H_{ad}$; Tafel step: $2H_{ad} \leftrightarrow H_2 + 2*$), which is in good agreement with the fact that HER/HOR mechanism on Pd does not change in universal pH solutions.[54] Since the proton is involved in the Volmer step (RDS) as either a reactant or a product, proton transfer is expected to affect its kinetics.

We further determined the specific exchange current density ($j_{0,s}$) of HER/HOR using Butler−Volmer linear fitting (Figure S8) in the micropolarization regions with an assumption of $\alpha_{a\text{-HOR}} + \alpha_{c\text{-HER}} = 1$, normalized by electrochemical surface area (ECSA) of Pd.[53] In an acidic solution (0.1 M $HClO_4$), the $j_{0,s}$ of HOR/HER was increased by up to 3.3 times over baseline Pd/C when metal oxides were introduced, following the trend of Pd/MoO_3/C (1.10 mA cm^{-2}_{Pd}) > Pd/WO_3/C (0.72 mA cm^{-2}_{Pd}) > Pd/ZrO_2/C (0.62 mA cm^{-2}_{Pd}) > Pd/CeO_2/C (0.37 mA cm^{-2}_{Pd}) > Pd/C (0.33 mA cm^{-2}_{Pd}) (Figure 2d). The HOR/HER activity trend aligns well with the surface acidity trend of metal oxides, i.e., MoO_3 > WO_3 > ZrO_2 > CeO_2 (Figure S9, metal oxide surface acidity correlation to their pK_a value), and the metal oxide with a pK_a value closer to the pH of electrolyte solution, i.e., smaller $\Delta = |pK_a - pH|$ leads to a larger enhancement of activity. Similar activity enhancement phenomena were observed in neutral and alkaline electrolyte

https://doi.org/10.1021/jacs.3c06398
J. Am. Chem. Soc. XXXX, XXX, XXX−XXX

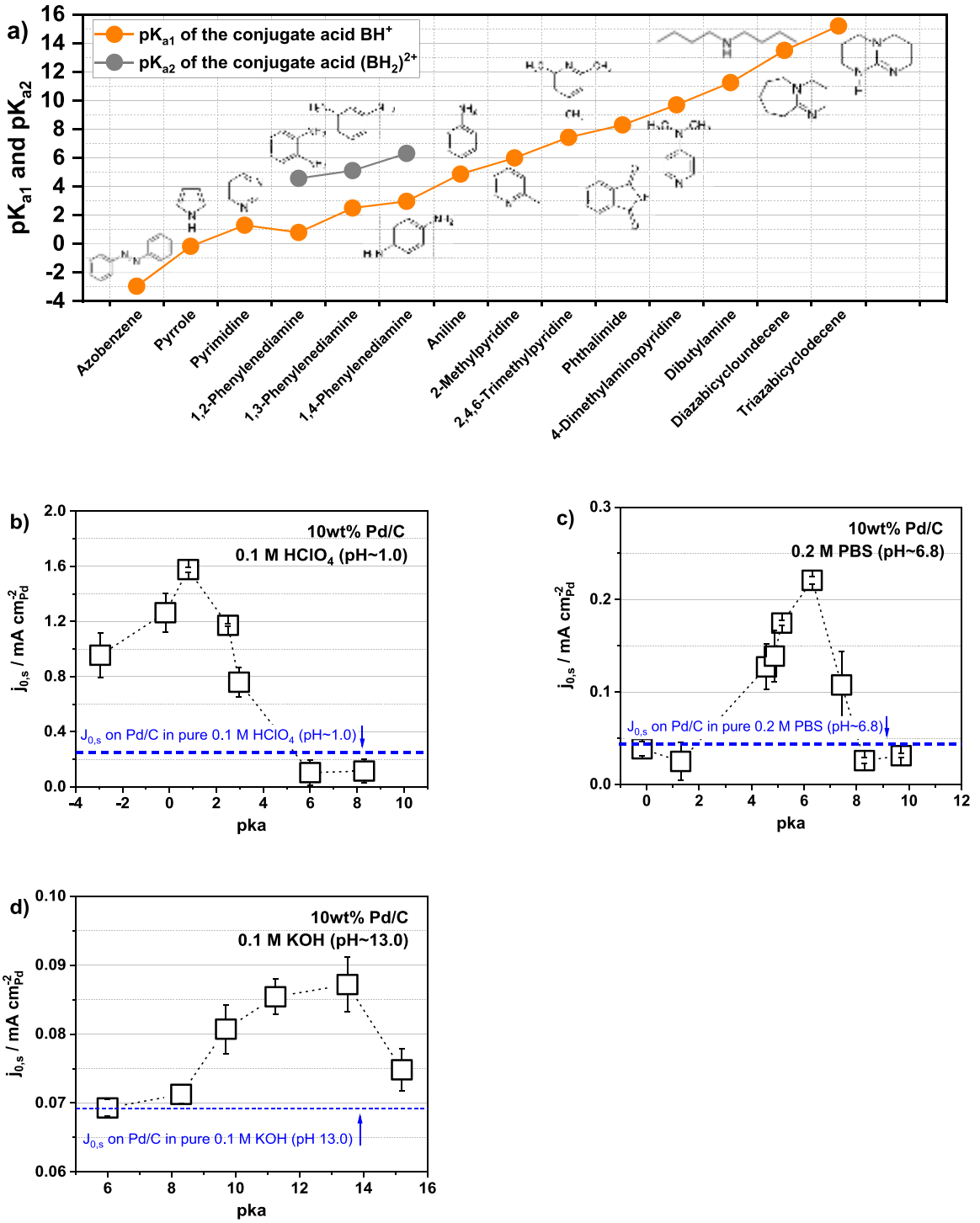

Figure 4. Amine additive effect. (a) pK_a values of amine molecules used in this work, (b–d) Volcano relationship of the HOR/HER rate enhancement as a function of the pK_a of amine additives in (b) 0.1 M HClO4 (pH ~ 1.1), (c) 0.2 M PBS (pH ~ 6.8), and (d) 0.1 M KOH (pH ~ 13.0).

solutions, with the maximum enhancement by 4.1 times (in neutral solution) and 4.9 times (in alkaline solution), respectively, both of which feature the smallest Δ (Figure 2e,f).

There are potentially several key factors that may influence the reaction kinetics: (1) proton transfer rate, (2) hydrogen adsorption strength on Pd, (3) the hydrophilicity/hydrophobicity, and (4) electron transfer rate. We first looked at the hydrophilicity/hydrophobicity; we measured the contact angles of Pd/C and Pt/MO/C. The contact angle of Pd/MO/C is larger than that of Pd/C (Figure S10, MO = MoO_x as an example), indicating that hydrophilicity is not the reason for enhanced electrocatalytic activity. We then studied the electron transfer rates through ferri/ferrocyanide measurements, from which we did not see any peak separation changes for electrodes with/without a metal oxide, indicating that the electron transfer rate was not changed (Figure S11).

We further calculated hydrogen adsorption energy (ΔG^0_H) on Pd for each sample using the peak position of hydrogen

https://doi.org/10.1021/jacs.3c06398
J. Am. Chem. Soc. XXXX, XXX, XXX−XXX

desorption peaks in the underpotentially deposited hydrogen (H_{upd}) region in cyclic voltammograms (Figures S12 and S13).[54] Similar ΔG^0_H values were obtained for Pd/C and Pd/MO/C samples in the same electrolyte (Figure S12), which indicates that the negligible ΔG^0_H change between them, and therefore the effect of hydrogen adsorption energy on HOR/HER activity change, can be eliminated. Note that on pristine Pd/C, the ΔG^0_H increases with solution pH, leading to decreased HER/HOR activities from an acidic to an alkaline electrolyte. This is in good agreement with previous results in the literature that show that a higher apparent hydrogen binding strength of Pd in alkaline electrolytes leads to lower HER/HOR activity in base than in acid.[51,54]

We then measured the activation energy (Figure S14). Pd/MoO_3/C shows a much smaller activation energy of 10.7 kJ mol^{-1} than Pd/C (29.4 kJ mol^{-1}) in an acidic electrolyte, while Pd/CeO_2/C exhibits the lowest activation of 19.9 kJ mol^{-1} among all Pd/C and Pd/MO/C samples in alkaline solution. Given the same HER/HOR reaction mechanisms (e.g., the Volmer step being the RDS) and similar hydrogen adsorption energies obtained between Pd/C and Pd/MO/C samples, the change of measured activation energy is mainly attributed to proton transfer energy barrier change where the lower activation energy implies a lower proton transfer energy barrier in the presence of metal oxides.

DFT computation results agree with the lower proton transfer energy barrier on the Pd/MO/C samples. For Volmer proton transfer directly from H_3O^+ in the electrolyte solution to the Pd surface, an energy barrier of 1.41 eV is determined using the model of Pd NPs on graphene oxide support (GO) (Figure 3a). When a MoO_3 particle is introduced into the same model, the proton is expected to transfer against the MoO_3 surface with hydrogen bond formation and cleavage to the Pd surface (i.e., proton transfer against μ^2-O sites of MoO_3). It should be noted that protons from the terminal O sites of MoO_3 are extremely basic and will not take part in the Volmer reaction (see discussions in the Supporting Information), and the maximum energy barrier of the new Volmer step (eq 10) decreases to 1.12 eV (Figure 3b). We further calculated the rate enhancement and its dependence on different factors: (a) the number and proximity of empty Pd sites around the MoO_3 sites (as shown in eq 13) and (b) the difference in the energy barrier ($\Delta\Delta E‡$) term (as shown in eq 14). The DFT calculation results reveal that the rate enhancement (Figure 3c) due to the MoO_3 sites is maximum around pH 3, almost equal to the $pK_{a(DFT)}$ = 3.08 of μ^2-oxygen of MoO_3 sites, which is consistent with the effect of proton relay in heterogeneous electrocatalysis. Experimental results confirm the trend of the rate enhancement (Figure 3d). It should be noted that the rate enhancement increases with the available Pd sites around the MoO_3 sites, i.e., the amount of Pd/MoO_3 interfaces (Figure S21), consistent with our previous experimental observation.[55]

To show the ubiquity of this phenomenon, we further simulated the Volmer reaction in the basic medium in the presence and absence of CeO_2 which has an experimental pK_a of 7.0−10.5. Similar to the GO-PdH-MoO_3 case, we also observed that the reaction energy barrier for the GO-PdH-CeO_2 case is lower by 0.12 eV (see Figure S16) than that of the GO-PdH-base case. For the GO-PdH-CeO_2 case, the maximum rate enhancement (Figure 3c) is seen around pH = 8, which is close to the computed $pK_{a(DFT)}$ of 7.4 for CeO_2. This confirms that the proton relay in heterogeneous electrocatalysis can be controlled as a function of pH using different metal oxides with different pK_a values. It should be noted that, for the GO-PdH-CeO_2 system, in our experiment, the highest rate enhancement is observed around pH = 13 (Figure 3d), which is not reproduced in our current theory model. There are several terminal and bridging (μ^2/μ^3) oxygen(s) present in the CeO_2 clusters that may have higher basicity; hence, proton transfer from these sites will become active at higher pHs.

Additionally, a small change (e.g., 0.1 eV) in $\Delta\Delta E‡$ can lead to a large variance (1 order of magnitude) in the absolute rate enhancement factor due to the exponential relationship in eq 14. We performed a sensitivity analysis to show how different values of $\Delta\Delta E‡$ can affect our result in an absolute case (Figure S21). We also showed the availability of unoccupied Pd sites near MoO_3 and CeO_2 sites affects the rate enhancement (Figures S22 and S23). It should be noted that the major point of our simulation is not to compute the absolute rate enhancement factor but rather to qualitatively understand at which pH the rate enhancement takes place for different metal oxides. Our simulation is not to be quantitative but rather to identify critical functionalities that can be used to design better catalysts.

In order to further investigate the proton relay effect on heterogeneous electrocatalysis, we used amine molecules with various pK_a values (ranging from −2.95 to 15.2, Figure 4a and Table S4) as additives in electrolytes to study a more precise relationship between pK_a (of additives), pH (of electrolyte solution), and activity enhancement. The HER/HOR activities were measured in the above three electrolytes of different pH with and without organic amine additives. To minimize solution pH change induced by the addition of amine molecules, an ultralow concentration of 0.1 mM amine additives was chosen. As shown in Figure 4b, a volcano-typed relationship was observed between the $j_{0,s}$ of HER/HOR and the pK_a value of organic amine additives in 0.1 M $HClO_4$, and the maximum HER/HOR activity enhancement for Pd/C is observed for 1,2-phenylenediamine with a pK_a of 0.8 ($j_{0,s}$ = 1.57 mA cm^{-2}_{Pd}), which has the smallest Δ. Similar volcano trends were observed in both 0.2 M PBS and 0.1 M KOH electrolytes (Figure 4c,d). The maximum HOR/HER kinetic enhancement is obtained from 1,4-phenylenediamine (pK_a = 6.31, $j_{0,s}$ = 0.22 mA cm^{-2}_{Pd}) and diazabicycloundecene (pK_a = 13.5, $j_{0,s}$ = 0.087 mA cm^{-2}_{Pd}) in neutral and alkaline electrolytes, respectively, both featuring the smallest Δ values. Although proton transfer behavior may be different between organic amine additives and metal oxides, the trends of HER/HOR activity enhancement are similar for both, strongly supporting the proton relay effect on reaction activity enhancement in acidic, neutral, and alkaline electrolytes.

It should be noted that, while the exact status of amine molecules on electrode surfaces is unknown, our electrochemical measurements indicate that amine molecules adsorb on the Pd (not on the carbon) surface. Cyclic voltammetry measurements show that hydrogen adsorption/desorption on Pd was suppressed with amine additives, indicating amine molecules occupy partial Pd surface (Figure S29). The electrochemical active surface area (ECSA) of Pd (measured via the CO-stripping method) decreases with amine additives, further indicating amine adsorbs on Pd (Figure S30 and Table S6). Our theoretical calculation reveals that the adsorption of amines of graphene oxide is not stable and amines move to the Pd nanoparticle. The calculated binding energy of an amine

https://doi.org/10.1021/jacs.3c06398
J. Am. Chem. Soc. XXXX, XXX, XXX−XXX

(pyrimidine) of Pd nanoparticle is −1.61 eV, indicating strong adsorption of pyrimidine on Pd (Figure S31).

We further apply electrocatalysts with a built-in metal oxide proton relay to other important proton-involved reactions: electrocatalytic hydrogenation (ECH) of benzaldehyde and electrocatalytic CO_2 reduction (CO_2RR). ECH of benzaldehyde follows the proton-coupled electron transfer mechanism on the Pd surface, and the overall ECH reaction rate (i.e., turnover frequency—TOF) has been reported to be significantly affected by proton transfer near the catalyst surface.[56] In our measurements (Figure S24), the TOF of benzaldehyde ECH increases up to approximately 3-fold on $Pd/WO_3/C$ in comparison to Pd/C, with the TOF on other catalysts following the order of $Pd/WO_3/C > Pd/MoO_3 > Pd/ZrO_2 > Pd/CeO_2 > Pd/C$, in which the metal oxide with pK_a closer to electrolyte solution pH (5.2) enables higher TOF improvement, similar to HER/HOR on these catalysts. On the other hand, we found that both the product selectivity and reaction activity of CO_2RR in CO_2-saturated 0.1 M $NaHCO_3$ (pH 6.8) are increased on Pd-ZrO_2/C in comparison to Pd/C (Figure S25). We chose Pd-ZrO_2/C because pK_a of ZrO_2 is close to the pH of the electrolyte solution.

CONCLUSIONS

In conclusion, we demonstrated that proton transfer can be tuned by metal oxide proton relay sites that are built within heterogeneous electrocatalyst architectures and amine molecules that adsorb on the metal catalyst surface, and the pK_a of proton relay sites allows the catalyst to respond optimally at a given solution pH, thereby tuning the kinetics of proton-involved electrocatalytic reactions. This study demonstrates a new approach to heterogeneous electrocatalyst design by incorporating proton relay sites into electrocatalyst architecture to control the proton-involved reaction kinetics.

METHODS

Catalyst Synthesis. *Synthesis of 2 wt % Metal Oxide (MO) on Carbon.* A portion (98 mg) of Vulcan XC 72R carbon black was treated by mixing with 0.2 mL of 0.5 M HCl, followed by air drying at room temperature for 24 h. A certain amount of $MoCl_5/WCl_6/ZrCl_6/Ce(NO_3)_3{\cdot}6H_2O$ was dissolved into anhydrous ethanol to form metal ethoxide and then mixed with pretreated 98 mg of carbon black with the target MO loading of 2 wt %. The mixture was dried at 60 °C, followed by step heat treatment in an Ar environment at 200 and 400 °C for 2 and 1 h, respectively. The ∼100 mg of MO/C sample was finally collected, followed by Pd deposition.

Synthesis of 5 wt % Pd/2 wt % MO/C. Solution A is prepared by dissolving 18.9 mg of K_2PdCl_6 into 15 mL of ethylene glycol with sonication for 15 min, followed by mixing with 95 mg of MO/C in a 100 mL styled round flask with an additional 30 min sonication. Solution B is prepared by dissolving 4.0 mg of NaOH into 10 mL of ethylene glycol with sonication for 15 min. Then, solution B was added to solution A and stirred at under 400 rpm rotation rate for 30 min. The mixture was transferred to an 80 mL glass microwave tube, which was microwave-treated (CEM Discover SP) at a constant 300 W for 3 min. The Pd/MO/C was collected via filtration and washed by using 1 L of deionized water (18.2 MΩ), followed by drying at 60 °C in a vacuum oven for 12 h.

Physicochemical Characterization. Powder X-ray diffraction (XRD) patterns were obtained with a Rigaku MiniFlex II X-ray generator with monochromatic Cu Kα radiation (λ = 1.54056 Å) at room temperature. The Pd and MO loading were analyzed using inductively coupled plasma optical emission spectroscopy (ICP-OES, PerkinElmer 7300DV OES with a cyclonic spray chamber and Meinhardt nebulizer), calibrated daily with NIST traceable standards, and cross-checked with independent NIST traceable standards. X-ray photoelectron spectroscopy (XPS) measurements were performed with a Physical Electronics Quantera Hybrid Scanning X-ray Microprobe. Infrared spectroscopic analysis of adsorbed pyridine (Py-IR) (Bruker Tensor 27 FTIR spectrometer) was used to determine the Brønsted acid and Lewis acid sites on the metal oxide surface.

Electrochemical Measurements. All electrochemical measurements were conducted in a three-electrode system using an electrochemical potentiostat (SP-300, Bio-Logic). A graphite carbon rod, which was isolated by a fritted glass tube from the main test electrolyte, and a Ag/AgCl electrode (Hg/HgO electrode is used in alkaline electrolytes) were used as the counter and the reference electrode, respectively. The working electrodes were catalyst (Pd/C or Pd/MO/C)-coated glass carbon electrodes. To fabricate the working electrode, a 2.0 mg mL^{-1} of catalyst ink was prepared by adding Pd/C or Pd/MO/C powders in H_2O/iso-propanol (IPA) with the ratio of 3:7 and 5% Nafion solution with the ratio of $8_{cat}{:}2_{Nafion}$, followed by 30 min of ultrasonication to fully disperse particles in the solvent. The catalyst ink was drop-casted onto the glassy carbon electrode surface (i.e., rotating disk electrode, RDE) with a Pd loading of 8/10/15 μg_{Pd} cm^{-2} for the HER/HOR polarization curve measurements in 0.1 M $HClO_4$, 0.2 M PBS, and 0.1 M KOH, respectively. After 30 min of air drying at ambient temperature, a uniform catalyst thin film was obtained for the following electrochemical measurements.

The Ag/AgCl reference electrode was calibrated prior to electrochemical measurements. Two Pt wires and Ag/AgCl electrodes were used as the working, counter, and reference electrodes, respectively. The 0.1 M $HClO_4$ solution (pH ≈ 1.0) was purged with ultrahigh-purity H_2 for at least 30 min before calibration to obtain H_2-saturated electrolyte, and the linear sweep voltammetry (LSV) test was conducted at a scan rate of 0.5 mV s^{-1} with a potential window of OCV ± 20 mV to determine the thermodynamic potential for H_2 evolution and oxidation reaction. We report all potentials against the reversible hydrogen electrode (RHE) in this study, which was converted from the potential vs Ag/AgCl by using eq 1.

$$E_{RHE} = E_{Ag/AgCl} + \Delta E \quad (1)$$

where ΔE equals 0.260 V in 0.1 M $HClO_4$ (pH ≈ 1.0) solution and 0.602 V in 0.2 M PBS (pH ≈ 6.8).

The Hg/HgO reference electrode was calibrated under the same protocol described above in 0.1 M KOH electrolyte, and the potential difference between Hg/HgO and the RHE is 0.980 V.

Electrochemical Impedance Spectroscopy. Electrochemical impedance spectroscopy (EIS) was conducted by applying an alternating current voltage with 10 mV amplitude at frequencies ranging from 300 kHz to 100 mHz. A Nyquist plot was obtained at open circuit voltage, and the measured solution resistance, R_s, was used to correct the practical potential applied on the working electrode using eq 2.

$$E_{iR-corrected} = E_{applied} - iR_s \quad (2)$$

where $E_{applied}$ is the applied potential on the working electrode, i is the corresponding measured current, R_s is the compensated electrolyte resistance determined by EIS, and $E_{iR\text{-corrected}}$ is the potential after iR-correction. The R_s of the three-electrode system was measured to be ∼15/∼50/∼40 Ω, in 0.1 M $HClO_4$, 0.2 M PBS, and 0.1 M KOH, respectively. All applied potentials in this study were reported versus the RHE after iR-correction.

HER/HOR Activity Measurement. Before each measurement, the working electrode was first cycled for at least 50 cycles (100 mV/s) under Ar purging to obtain stable CV curves. Then, the HER/HOR performance was measured at room temperature with an RDE rotating rate of 1600 rpm. The electrolyte was purged with UHP H_2 gas for at least 30 min prior to tests to obtain an H_2-saturated electrolyte. It is important to note that H_2 could be absorbed into the Pd lattice, thereby showing an extra HOR peak in its corresponding polarization curve. Thus, we used a low scan rate of 1 mV s^{-1} to reveal the intrinsic activity of Pd-based catalysts. In addition, to avoid H_2

https://doi.org/10.1021/jacs.3c06398
J. Am. Chem. Soc. XXXX, XXX, XXX−XXX

bubble coverage during the HER process, the LSV was conducted from −0.1 to 0.9 V vs RHE for the HER/HOR polarization curve collection.

To study the effect of amine additives, the electrolytes were prepared by adding 0.1 mM amine organics into the H_2-saturated electrolyte with a RDE rotating of 1600 rpm for 5 min, followed by HER/HOR measurement under the same conditions described above. It should be noted that the solubility of azobenzene is smaller than 0.1 mM. We prepared 0.03 mM of the azobenzene electrolyte, while other amines kept the concentration of 0.1 mM.

To determine the specific exchange current density of HER/HOR on Pd-based catalyst, the kinetic current of HER/HOR, ik was calculated based on the Koutecky−Levich equation.

$$\frac{1}{i} = \frac{1}{ik} - \frac{1}{id} \tag{3}$$

where id is the measured diffusion limiting current.

The exchange current, i_0, was determined by using eq 4 in micropolarization regions of ±20 to ±50 mV vs RHE. The ik and overpotential, η, can be fitted into the linearized Butler−Volmer equation with the assumption that the summation of anodic and cathodic transfer coefficient equals 1, ($\alpha_a + \alpha_c = 1$).

$$ik = i_0 \frac{F\eta}{RT} \tag{4}$$

where F is the Faraday constant, R is the molar gas constant, and T is the operating temperature. i_0 was then normalized by the electrochemical surface area (ECSA) of Pd to obtain the specific exchange current density, $j_{0,s}$ with a unit of mA cm^{-2}_{Pd}. See "S5. Electrochemical Surface Area Measurement by the CO-Stripping Method" for ECSA measurement.

To study the accuracy of linearly fitted i_0, the i_0 values were fitted back into the Butler−Volmer equation of eq 5, and $\alpha_{a(HOR)}$ and $\alpha_{c(HER)}$ were also obtained. The R-squared value was obtained higher than 99.1% and reported in this work (Figure S17).

$$ik = i_0\left(\exp\left(\frac{\alpha_a F\eta}{RT}\right) - \exp\left(-\frac{\alpha_c F\eta}{RT}\right)\right) \tag{5}$$

Electrochemical Surface Area Measurement by the CO-Stripping Method. The electrochemical surface area (ECSA) of Pd in Pd/C and Pd/MO/C was determined using CO-stripping voltammograms. The Pd/C or Pd/MO/C electrode was first cycled at a scan rate of 100 mV/s for at least 50 cycles under Ar purging to obtain a stable CV. Afterward, the electrolyte was purged with CO for 20 min to obtain a CO-saturated solution. The electrode was subsequently held at 0.3 V vs RHE for 15 min in a CO-saturated solution, followed by another 15 min with Ar purging. The CV was then conducted between 0.3 and 1.20 V vs RHE with a 20 mV/s scan rate. During the positive scanning (electrode potential goes from low to high), the adsorbed CO is oxidized, and the corresponding CO oxidation peak is observed from the first cycle of CO-stripping voltammograms. After 1 cycle scanning, the adsorbed CO should be completely removed, and the total charge difference between the first and second cycles (total charge of adsorbed CO oxidation) can be used for active metal ECSA determination by using the following equation.

$$\mathrm{ECSA_{Pd}} = \frac{Q}{420\ \mu\mathrm{C\ cm^{-2}} \times m} \tag{6}$$

where Q is the total charge of adsorbed CO oxidation, m is the total loading of Pd, and the 420 μC cm^{-2} corresponds to a monolayer of adsorbed CO. The ECSA of Pd for 5 wt % Pd/C, Pd/MoO_3/C, Pd/WO_3/C, Pd/ZrO_2/C, and Pd/CeO_2/C samples was measured in 0.1 M $HClO_4$ (Table S5).

The ECSA of Pd for the Pd/C sample was also measured in 0.1 M $HClO_4$, 0.2 M PBS, and 0.1 M KOH electrolyte with and without 0.1 mM organic amine additives. Three working electrodes, i.e., RDE, were prepared using the same Pd/C catalyst ink for ECSA and HER/HOR activity determination, respectively. The ECSA of Pd is first measured in the electrolyte without amine additives using RDE#1; the ECSA of Pd is then determined in the electrolyte with amine additives using RDE#2; the RDE#3 is used to collect HER/HOR performance in the electrolyte with and without amine additive addition. The ECSA of Pd decreases when amine additives are introduced (i.e., $\mathrm{ECSA_{RDE\#1}} > \mathrm{ECSA_{RDE\#2}}$), indicating the Pd surface coverage by organic amine additives. The $\mathrm{ECSA_{RDE\#2}}$ will be directly used for $j_{0,s}$ calculation of the HER/HOR (HER/HOR polarization curve from RDE#3) without ECSA calibration. Since the measured $\mathrm{ECSA_{RDE\#1}}$ could slightly vary due to ink dispersion and RDE thin film catalyst layer drying difference, we reported the $\mathrm{ECSA_{RDE\#2}}$ results of Pd for 10 wt % Pd/C in Table S6 after the correction by multiplying correction constant (x) obtained from $\mathrm{ECSA_{RDE\#1}}$ difference for each amine additive testing (i.e., $x = \mathrm{ECSA_{RDE\#1}} - \mathrm{amine\#1/ECSA_{RDE\#1}} - \mathrm{amine\#2}$).

Computational Methods and Models. Ab initio molecular dynamics (AIMD) simulations were performed using the PBE functional[57] along with Grimme D3 dispersion correction[58] using the CP2K software package.[59] Canonical NVT ensemble simulations at 400 K were performed, followed by a simulated annealing (SA) process to get the lowest energy structure. Norm conserving pseudopotentials were used for core electrons[60] and DZVP quality Gaussian type basis sets were used for all atoms except Ce; for Ce, a DZV quality basis set was used. An auxiliary plane-wave basis set with 400 Ry cutoff criteria was used for calculating electrostatic terms.[61] Γ-point approximation was used for Brillouin zone sampling. Starting from the structure reported in the literature,[56] we simulated the GO-PdH system which contains one layer of graphene oxide (functionalized with COOH and OH group), Pd nanocluster with 50 Pd atoms (with 24 hydrogen atoms occupying the hollow sites of Pd nanocluster) and 162 water molecules (see Figure S16). For GO-PdH systems with MOs we added $(MoO_3)_3$ and $(CeO_2)_3$ trimer on top of the above-mentioned system (see Figures S18 and S19) and performed the AIMD simulation followed by the SA process to obtain the lowest energy structure of the GO-PdH-MoO_3 and GO-PdH-CeO_2 system. The reaction barrier for the Volmer reaction was computed by constraining the position of hydrogen(s) involved in the reaction. Thus, our computed reaction barriers are an approximate transition state which is the upper limit of the actual reaction barrier of the process. This means that the rates computed using these barriers will be lower than the actual rate of the reaction observed experimentally.

Furthermore, to model the electrochemistry in an acid medium, we added H^+ (i.e., added proton to bulk water) and Cl^- counterion in our system GO-PdH (GO-PdH-acid) and GO-PdH-MoO_3 system and optimized using density functional theory (DFT). It should be noted that experimentally, $HClO_4$ was used in the acidic electrolyte solution. In our model, we used HCl in order to simplify our modeling effort. The Volmer reaction for the GO-PdH-acid system is following:

$$\text{Volmer Step: } H_3O^+ + e^- + \mathrm{Pd} \leftrightarrow \mathrm{PdH} + H_2O \tag{7}$$

The Gibbs free energy (ΔG) of the Volmer reaction in acid medium can be expressed as follows:

$$\Delta G = \Delta E + 2.303 k_B T \times \mathrm{pH} - T\Delta S \tag{8}$$

where ΔG is the Gibbs free energy difference of the reaction, ΔE is the electronic energy difference of the reaction, k_B is Boltzmann constant, T is temperature, pH is the strength of acidity of the solution, and ΔS is the change in entropy of the reactant and product.

For the Volmer reaction, the ΔG value of the process depends on the pH of the solution. However, the ΔS term is rather small as we are breaking one O−H bond and forming a Pd−H bond. Hence, for the Volmer reaction, the effect of pH should be considered while computing the reaction free energy. However, the pH term is a linear term and will be similar for the GO-PdH-acid and GO-PdH-MoO_3 system and thus neglected in Figure 3 in the main manuscript.

https://doi.org/10.1021/jacs.3c06398
J. Am. Chem. Soc. XXXX, XXX, XXX−XXX

The overall rate of the Volmer reaction for the GO-PdH-acid system is as follows:

$$r(\mathrm{GO-PdH-acid}) = k_{\mathrm{H_3O^+}}[\mathrm{H_3O^+}][\mathrm{Pd}] \quad (9)$$

where r(GO-PdH-acid) is the rate of the Volmer reaction for the GO-PdH-acid system. $k_{\mathrm{H3O+}}$ is the rate constant of the Volmer reaction from the bulk water, and $[\mathrm{H_3O^+}]$ and [Pd] are concentrations of available protons and empty Pd sites where $\mathrm{H^+}$ and electrons can move from bulk water to the Pd surface.

In the presence of GO-PdH-MoO_3, the Volmer reaction is as follows:

$$\text{Volmer Step: } (\mathrm{MoO_3})\mathrm{H^+} + \mathrm{e^-} + \mathrm{Pd} \leftrightarrow \mathrm{PdH} + \mathrm{MoO_3} \quad (10)$$

The Volmer reaction from the MoO_3 site depends on the proton transfer from bulk water to the oxygens (Figure S20) of MoO_3:

$$\mathrm{MoO_3} + \mathrm{H_3O^+} \leftrightarrow (\mathrm{MoO_3})\mathrm{H^+} + \mathrm{H_2O} \quad (11)$$

This is a pH-dependent process, and relative occupation of MoO_3 and (MoO_3)-H^+ is governed by the Henderson−Hasselbalch equation (Figure S15a). Moreover, in the presence of MO, the Volmer reaction can also happen directly from bulk water similar to the GO-PdH-acid system. Thus, the overall reaction rate for the Volmer process for the GO-PdH-MoO_3 system is the following:

$$r(\mathrm{GO-PdH-MoO_3}) = k_{\mathrm{H_3O^+}}[\mathrm{H_3O^+}][\mathrm{Pd}] \times y + k_{(\mathrm{MoO_3})-\mathrm{H^+}}[(\mathrm{MoO_3}) - \mathrm{H^+}][\mathrm{Pd}] \times x \quad (12)$$

where r(GO-PdH-MoO_3) is the rate of the overall Volmer reaction in the presence of MoO_3. $k_{\mathrm{H3O+}}$ and $k_{(\mathrm{MoO3})\text{-H+}}$ are the rate constants of the Volmer reaction from the bulk water and protonated MoO_3 sites, respectively. $[\mathrm{H_3O^+}]$ and $[(\mathrm{MoO_3})\text{-}\mathrm{H^+}]$ are concentrations of protonated water and MoO_3 sites, respectively, and [Pd] is the concentration of empty Pd sites where $\mathrm{H^+}$ and electrons can move during the Volmer reaction. $x + y = 1$ and x and y represent the fraction of empty Pd sites that are close to MO and water, respectively.

The concentration of Pd (empty sites shown on (Figure S15b) in the second term of eq 12 will depend on not only the proximity but also the probability Volmer reaction from the bulk water. At a high acid concentration, the Pd sites can take H directly from bulk water, thereby reducing the rate enhancement due to MoO_3 sites. The rate enhancement due to MoO_3 sites comes from the second term of eq 12.

Thus, the overall rate enhancement due to MoO3 can be written as the ratios of eqs 12 and 9

$$\text{rate enhancement factor} = y + \frac{k_{\mathrm{MoO_3}-\mathrm{H^+}} \times [(\mathrm{MoO_3}) - \mathrm{H^+}][\mathrm{Pd}] \times x}{k_{\mathrm{H_3O^+}}} \quad (13)$$

In eq 13, the ratio of $k_{\mathrm{H_3O^+}}$ and $k_{(\mathrm{MoO_3})-\mathrm{H^+}}$ can be roughly estimated from the Arrhenius equation $\left(k = A \times \exp\left(\frac{-\Delta G^{\ddagger}}{k_B T}\right)\right)$, where A is the pre-exponential rate factor, $\Delta G^{\ddagger}$ is the reaction energy barrier for the Volmer step, k_B is the Boltzmann constant, and T is the temperature of the reaction. Assuming the pre-exponential factor A and entropy term ($T\Delta S$) to be equal for both $k_{\mathrm{H_3O^+}}$ and $k_{(\mathrm{MoO_3})-\mathrm{H^+}}$, the ratio of the rate constants can be approximated as follows:

$$\frac{k_{\mathrm{MoO_3}-\mathrm{H^+}}}{k_{\mathrm{H_3O^+}}} = \exp\left(\frac{-\Delta\Delta E^{\ddagger}}{k_B T}\right) \quad (14)$$

where $\Delta\Delta E^{\ddagger}$ is the electronic energy difference of the Volmer reaction energy barrier from the MoO_3 site and bulk water, respectively.

To model the Volmer reaction in the basic medium, we added a Na atom in our GO-PdH system (which will be referred to as GO-PdH-base) which acts as the source of electrons, as shown in the reaction mechanism below. The addition of the Na atom acts as the proxy of free electrons from the electrode. The Volmer reaction in the presence of base is as follows:

$$\text{Volmer Step: } \mathrm{H_2O} + \mathrm{e^-} + \mathrm{Pd} \leftrightarrow \mathrm{PdH} + \mathrm{OH^-} \quad (15)$$

The reaction free energy (ΔG) of the Volmer reaction in the presence of base can be written as follows:

$$\Delta G = \Delta E - 2.303 k_B T \times p\mathrm{OH} - T\Delta S \quad (16)$$

where ΔG is the Gibbs free energy difference of the reaction, ΔE is the electronic energy difference of the reaction, k_B is Boltzmann constant, T is temperature, pOH is the strength of basicity of the solution, and ΔS is the change in entropy of the reactant and product.

For the Volmer reaction, the ΔG of the process depends on the pOH of the solution. However, the ΔS term is rather small as we are breaking one O−H bond and forming a Pd−H bond. Hence, for the Volmer reaction, the effect of pOH should be considered in the reaction free energy. However, the effect of pOH is the same for the GO-PdH-base and GO-PdH-CeO_2 systems and hence neglected in Figure S15.

The Volmer reaction rate for the GO-PdH-base system is the following:

$$r(\mathrm{GO-PdH-base}) = k_{\mathrm{H_2O}}[\mathrm{H_2O}][\mathrm{Pd}] \quad (17)$$

Similar to the GO-PdH-base system, we also added a Na atom to the GO-PdH-CeO_2 system, then computer Volmer reaction pathways for the GO-PdH-CeO_2 system. The Volmer reaction for the GO-PdH-CeO_2 system is as follows:

$$\text{Volmer Step: } (\mathrm{CeO_2})\mathrm{H} + \mathrm{e^-} + \mathrm{Pd} \leftrightarrow \mathrm{PdH} + (\mathrm{CeO_2})^- \quad (18)$$

Note that during our *NVT* simulation, two of the bulk water molecules dissociated on the $(CeO_2)_3$ cluster and protonated one terminal and one μ^2 oxygen of the $(CeO_2)_3$ cluster. This is consistent with the fact that CeO_2 is a basic oxide. These protons can further participate in the Volmer reaction, as shown in the reaction step above.

The Volmer reaction from the CeO_2 site depends on the pOH of the overall system. Under strong basic conditions, the μ^2 oxygen sites will no longer remain in the protonated state; hence, the Volmer reaction will not happen. The deprotonation of the (CeO_2)-H sites happens using the following chemical reaction:

$$(\mathrm{CeO_2})\mathrm{H} + \mathrm{OH^-} \leftrightarrow (\mathrm{CeO_2})^- + \mathrm{H_2O} \quad (19)$$

The relative ratio of protonated versus deprotonated CeO_2 sites also depends on the pH/pOH of the system and is governed by the Henderson−Hasselbalch equation.

Similar to the MoO_3 case, in the presence of the CeO_2, the Volmer reaction can also happen directly from bulk water as in the GO-PdH-base system. Thus, the overall reaction rate for the Volmer process for the GO-PdH-CeO_2 system is as follows:

$$r(\mathrm{GO-PdH-CeO_2}) = k_{\mathrm{H_2O}}[\mathrm{H_2O}][\mathrm{Pd}] \times y + k_{(\mathrm{CeO_2})-\mathrm{H}}[(\mathrm{CeO_2}) - \mathrm{H}][\mathrm{Pd}] \times x \quad (20)$$

where r(GO-PdH-CeO_2) is the rate of the overall Volmer reaction in the presence of CeO_2. k_{H2O} and $k_{(\mathrm{CeO2})\text{-H}}$ are the rate constants of the Volmer reaction from the bulk water and protonated CeO_2 sites, respectively. $[\mathrm{H_2O}]$ and $[(\mathrm{CeO_2})\text{-H}]$ are the concentrations of available water and CeO_2 sites from which $\mathrm{H^+}$ for the Volmer reaction can be abstracted, [Pd] is the concentration of empty Pd sites where $\mathrm{H^+}$ and electrons can move during the Volmer reaction, and y and x are fraction of empty Pd sites near bulk water and CeO_2, respectively

https://doi.org/10.1021/jacs.3c06398
J. Am. Chem. Soc. XXXX, XXX, XXX−XXX

$(y + x = 1)$. Thus, the overall rate enhancement factor for the GO-PdH-CeO_2 system can be expressed as follows:

$$\text{rate enhancement factor} = y + \frac{k_{CeO_2-H} \times [(CeO_2) - H][Pd] \times x}{k_{H_2O}} \quad (21)$$

In eq 21, the ratio of k_{CeO_2-H} and k_{H_2O} can be estimated using the following equation:

$$\frac{k_{CeO_2-H}}{k_{H_2O}} = \exp\left(\frac{-\Delta\Delta E^{\ddagger}}{k_B T}\right) \quad (22)$$

It should be noted that the reference state of the catalyst in acid and basic media is different; therefore, relative energetics of the reactions of the GO-PdH-acid and GO-PdH-base cannot be compared directly without factoring in the shift of the reference state. To simplify this comparison, we compared the GO-PdH-acid with GO-PdH-MoO_3 and GO-PdH-base with GO-PdH-CeO_2 systems directly.

■ ASSOCIATED CONTENT

Supporting Information

The Supporting Information is available free of charge at https://pubs.acs.org/doi/10.1021/jacs.3c06398.

Chemicals used in experiments; TEM, XRD, XPS, and IR spectra; contact angle results; pK_a values; computational details and results for geometry optimizations and energy calculation; cyclic voltammograms; and electrochemical measurement results (PDF)

■ AUTHOR INFORMATION

Corresponding Authors

Roger Rousseau − *Pacific Northwest National Laboratory, Richland, Washington 99352, United States;* Present Address: Chemical Science Division, Oak Ridge National Laboratory, Oak Ridge, Tennessee 37830, United States; orcid.org/0000-0003-1947-0478; Email: rousseaur@ornl.gov

Yuyan Shao − *Pacific Northwest National Laboratory, Richland, Washington 99352, United States;* orcid.org/0000-0001-5735-2670; Email: yuyan.shao@pnnl.gov

Authors

Yang Qiu − *Pacific Northwest National Laboratory, Richland, Washington 99352, United States*

Debmalya Ray − *Pacific Northwest National Laboratory, Richland, Washington 99352, United States;* Present Address: Chemical Science Division, Oak Ridge National Laboratory, Oak Ridge, Tennessee 37830, United States

Litao Yan − *Pacific Northwest National Laboratory, Richland, Washington 99352, United States*

Xiaohong Li − *Pacific Northwest National Laboratory, Richland, Washington 99352, United States*

Miao Song − *Pacific Northwest National Laboratory, Richland, Washington 99352, United States*

Mark H. Engelhard − *Pacific Northwest National Laboratory, Richland, Washington 99352, United States;* orcid.org/0000-0002-5543-0812

Junming Sun − *Voiland School of Chemical Engineering and Bioengineering, Washington State University, Pullman, Washington 99164, United States*

Mal-Soon Lee − *Pacific Northwest National Laboratory, Richland, Washington 99352, United States;* orcid.org/0000-0001-6851-177X

Xin Zhang − *Pacific Northwest National Laboratory, Richland, Washington 99352, United States;* orcid.org/0000-0003-2000-858X

Manh-Thuong Nguyen − *Pacific Northwest National Laboratory, Richland, Washington 99352, United States;* orcid.org/0000-0003-1997-0368

Vassiliki-Alexandra Glezakou − *Pacific Northwest National Laboratory, Richland, Washington 99352, United States;* Present Address: Chemical Science Division, Oak Ridge National Laboratory, Oak Ridge, Tennessee 37830, United States; orcid.org/0000-0001-6028-7021

Yong Wang − *Pacific Northwest National Laboratory, Richland, Washington 99352, United States; Voiland School of Chemical Engineering and Bioengineering, Washington State University, Pullman, Washington 99164, United States;* orcid.org/0000-0002-8460-7410

Complete contact information is available at: https://pubs.acs.org/10.1021/jacs.3c06398

Notes

The authors declare no competing financial interest.

The views and opinions of the authors expressed herein do not necessarily state or reflect those of the US Government or any agency thereof. Neither the US Government nor any agency thereof, nor any of their employees, makes any warranty, expressed or implied, or assumes any legal liability or responsibility for the accuracy, completeness, or usefulness of any information, apparatus, product, or process disclosed, or represents that its use would not infringe privately owned rights.

■ ACKNOWLEDGMENTS

The authors would like to acknowledge financial support from Chemical Transformation Initiative, a Laboratory Directed Research and Development Project at Pacific Northwest National Laboratory (PNNL) for materials synthesis, the US Department of Energy (DOE) Hydrogen and Fuel Cell Technology Office (Program Manager: Katie Randolph) for materials characterization and mechanisms study, and the US DOE Basic Energy Sciences, Chemical Sciences, Geosciences and Biosciences Division, Catalysis Program (FWP 47319) for DFT calculation study. The STEM and XPS measurements were performed at the William R. Wiley Environmental Molecular Sciences Laboratory, a national scientific user facility sponsored by the U.S. Department of Energy's Office of Biological and Environmental Research and located at PNNL. The computer resources were provided by the National Energy Research Center (NERSC) located at the Lawrence Berkeley National Laboratory (LBNL) and the PNNL Research Computing facility. PNNL is operated by Battelle for DOE under Contract DE-AC05-76RL01830. The authors thank Andrew T Pitman for language editing.

■ REFERENCES

(1) Greeley, J.; Jaramillo, T. F.; Bonde, J.; Chorkendorff, I. B.; Norskov, J. K. Computational high-throughput screening of electrocatalytic materials for hydrogen evolution. *Nat. Mater.* **2006**, *5* (11), 909−913.

(2) Feng, Q. C.; Wang, X. L.; Klingenhof, M.; Heggen, M.; Strasser, P. Low-Pt NiNC-Supported PtNi Nanoalloy Oxygen Reduction

Reaction Electrocatalysts-In Situ Tracking of the Atomic Alloying Process. *Angew. Chem., Int. Ed.* **2022**, *61* (36), No. e202203728.
(3) Lopes, P. P.; Li, D. G.; Lv, H. F.; Wang, C.; Tripkovic, D.; Zhu, Y. S.; Schimmenti, R.; Daimon, H.; Kang, Y. J.; Snyder, J.; Becknell, N.; More, K. L.; Strmcnik, D.; Markovic, N. M.; Mavrikakis, M.; Stamenkovic, V. R. Eliminating dissolution of platinum-based electrocatalysts at the atomic scale. *Nat. Mater.* **2020**, *19* (11), 1207−1214, DOI: 10.1038/s41563-020-0735-3.
(4) Gao, Y. F.; Uchiyama, T.; Yamamoto, K.; Watanabe, T.; Tominaka, S.; Thakur, N.; Sato, R.; Teranishi, T.; Imai, H.; Sakurai, Y.; Uchimoto, Y. Origin of High Activity and Durability of Confined Ordered Intermetallic PtCo Catalysts for the Oxygen Reduction Reaction in Rotating Disk Electrode and Fuel Cell Operating Conditions. *ACS Catal.* **2023**, *13* (16), 10988−11000.
(5) Li, J. R.; Sharma, S.; Wei, K. C.; Chen, Z. T.; Morris, D.; Lin, H. H.; Zeng, C.; Chi, M. F.; Yin, Z. Y.; Muzzio, M.; Shen, M. Q.; Zhang, P.; Peterson, A. A.; Sun, S. H. Anisotropic Strain Tuning of L1 < sub > 0</sub> Ternary Nanoparticles for Oxygen Reduction. *J. Am. Chem. Soc.* **2020**, *142* (45), 19209−19216.
(6) Yang, C. L.; Wang, L. N.; Yin, P.; Liu, J. Y.; Chen, M. X.; Yan, Q. Q.; Wang, Z. S.; Xu, S. L.; Chu, S. Q.; Cui, C. H.; Ju, H. X.; Zhu, J. F.; Lin, Y.; Shui, J. L.; Liang, H. W. Sulfur-anchoring synthesis of platinum intermetallic nanoparticle catalysts for fuel cells. *Science* **2021**, *374* (6566), 459−464.
(7) Calle-Vallejo, F.; Tymoczko, J.; Colic, V.; Vu, Q. H.; Pohl, M. D.; Morgenstern, K.; Loffreda, D.; Sautet, P.; Schuhmann, W.; Bandarenka, A. S. Finding optimal surface sites on heterogeneous catalysts by counting nearest neighbors. *Science* **2015**, *350* (6257), 185−189.
(8) Gao, G. P.; Sun, G.; Du, A. J. Activating Catalytic Inert Basal Plane of Molybdenum Disulfide to Optimize Hydrogen Evolution Activity via Defect Doping and Strain Engineering. *J. Phys. Chem. C* **2016**, *120* (30), 16761−16766.
(9) He, T.; Wang, W.; Shi, F.; Yang, X.; Li, X.; Wu, J.; Yin, Y.; Jin, M. Mastering the surface strain of platinum catalysts for efficient electrocatalysis. *Nature* **2021**, *598* (7879), 76−81.
(10) Strmcnik, D.; Uchimura, M.; Wang, C.; Subbaraman, R.; Danilovic, N.; van der Vliet, D.; Paulikas, A. P.; Stamenkovic, V. R.; Markovic, N. M. Improving the hydrogen oxidation reaction rate by promotion of hydroxyl adsorption. *Nat. Chem.* **2013**, *5* (4), 300−306.
(11) Wang, Y.; Gong, N.; Liu, H. F.; Ma, W.; Hippalgaonkar, K.; Liu, Z.; Huang, Y. Z. Ordering-Dependent Hydrogen Evolution and Oxygen Reduction Electrocatalysis of High-Entropy Intermetallic Pt < sub > 4</sub > FeCoCuNi. *Adv. Mater.* **2023**, *35* (28), No. 2302067.
(12) Kulkarni, A.; Siahrostami, S.; Patel, A.; Norskov, J. K. Understanding Catalytic Activity Trends in the Oxygen Reduction Reaction. *Chem. Rev.* **2018**, *118* (5), 2302−2312.
(13) Seitz, L. C.; Dickens, C. F.; Nishio, K.; Hikita, Y.; Montoya, J.; Doyle, A.; Kirk, C.; Vojvodic, A.; Hwang, H. Y.; Norskov, J. K.; Jaramillo, T. F. A highly active and stable IrO < i>_x</ i>/SrIrO < sub > 3</sub> catalyst for the oxygen evolution reaction. *Science* **2016**, *353* (6303), 1011−1014.
(14) Clark, E. L.; Hahn, C.; Jaramillo, T. F.; Bell, A. T. Electrochemical CO < sub > 2</sub> Reduction over Compressively Strained CuAg Surface Alloys with Enhanced Multi-Carbon Oxygenate Selectivity. *J. Am. Chem. Soc.* **2017**, *139* (44), 15848−15857.
(15) Qiao, Y.; Kastlunger, G.; Davis, R. C.; Rodriguez, C. A. G.; Vishart, A.; Deng, W. Y.; Xu, Q. C.; Li, S. F.; Benedek, P.; Chen, J. J.; Schroder, J.; Perryman, J.; Lee, D. U.; Jaramillo, T. F.; Chorkendorff, I.; Seger, B. Mechanistic Insights into Aldehyde Production from Electrochemical CO < sub > 2</sub> Reduction on CuAg Alloy < i > via Operando</i> X-ray Measurements. *ACS Catal.* **2023**, *13* (14), 9379−9391.
(16) Wang, T.; Zhang, Y.; Huang, B.; Cai, B.; Rao, R. R.; Giordano, L.; Sun, S.-G.; Shao-Horn, Y. Enhancing oxygen reduction electrocatalysis by tuning interfacial hydrogen bonds. *Nat. Catal.* **2021**, *4*, 753−762.
(17) Barrio, J.; Pedersen, A.; Favero, S.; Luo, H.; Wang, M. N.; Sarma, S. C.; Feng, J. Y.; Ngoc, L. T. T.; Kellner, S.; Li, A. Y.; Sobrido, A. B. J.; Titirici, M. M. Bioinspired and Bioderived Aqueous Electrocatalysis. *Chem. Rev.* **2022**, *123*, 2311−2348, DOI: 10.1021/acs.chemrev.2c00429.
(18) Dolui, D.; Khandelwal, S.; Shaik, A.; Gaat, D.; Thiruvenkatam, V.; Dutta, A. Enzyme-Inspired Synthetic Proton Relays Generate Fast and Acid-Stable Cobalt-Based H < sub > 2</sub> Production Electrocatalysts. *ACS Catal.* **2019**, *9* (11), 10115−10125.
(19) Tse, E. C. M.; Barile, C. J.; Kirchschlager, N. A.; Li, Y.; Gewargis, J. P.; Zimmerman, S. C.; Hosseini, A.; Gewirth, A. A. Proton transfer dynamics control the mechanism of O_2 reduction by a non-precious metal electrocatalyst. *Nat. Mater.* **2016**, *15* (7), 754−759.
(20) Gautam, R. P.; Lee, Y. T.; Herman, G. L.; Moreno, C. M.; Tse, E. C. M.; Barile, C. J. Controlling Proton and Electron Transfer Rates to Enhance the Activity of an Oxygen Reduction Electrocatalyst. *Angew. Chem.-Int. Ed.* **2018**, *57* (41), 13480−13483.
(21) Warburton, R. E.; Soudackov, A. V.; Hammes-Schiffer, S. Theoretical Modeling of Electrochemical Proton-Coupled Electron Transfer. *Chem. Rev.* **2022**, *122* (12), 10599−10650.
(22) Andrei, I. M.; Barboiu, M. Biomimetic Artificial Proton Channels. *Biomolecules* **2022**, *12* (10), 1473.
(23) Corbella, M.; Pinto, G. P.; Kamerlin, S. C. L. Loop dynamics and the evolution of enzyme activity. *Nat. Rev. Chem.* **2023**, *7* (8), 536−547.
(24) Fontecilla-Camps, J. C.; Volbeda, A.; Cavazza, C.; Nicolet, Y. Structure/function relationships of [NiFe]- and [FeFe]-hydrogenases. *Chem. Rev.* **2007**, *107* (10), 4273−4303.
(25) Schilter, D.; Camara, J. M.; Huynh, M. T.; Hammes-Schiffer, S.; Rauchfuss, T. B. Hydrogenase Enzymes and Their Synthetic Models: The Role of Metal Hydrides. *Chem. Rev.* **2016**, *116* (15), 8693−8749.
(26) Lin, S. Y.; Banerjee, S.; Fortunato, M. T.; Xue, C. C.; Huang, J.; Turro, C.; Sokolov, A. Y. Electrochemical Strategy for Proton Relay Installation Enhances the Activity of a Hydrogen Evolution Electrocatalyst. *J. Am. Chem. Soc.* **2022**, *144* (44), 20267−20277.
(27) Bullock, R. M.; Chen, J. G. G.; Gagliardi, L.; Chirik, P. J.; Farha, O. K.; Hendon, C. H.; Jones, C. W.; Keith, J. A.; Klosin, J.; Minteer, S. D.; Morris, R. H.; Radosevich, A. T.; Rauchfuss, T. B.; Strotman, N. A.; Vojvodic, A.; Ward, T. R.; Yang, J. Y.; Surendranath, Y. Using nature's blueprint to expand catalysis with Earth-abundant metals. *Science* **2020**, *369* (6505), No. eabc3183, DOI: 10.1126/science.abc3183.
(28) Costentin, C.; Drouet, S.; Passard, G.; Robert, M.; Saveant, J. M. Proton-coupled electron transfer cleavage of heavy-atom bonds in electrocatalytic processes. cleavage of a C-O bond in the catalyzed electrochemical reduction of CO_2. *J. Am. Chem. Soc.* **2013**, *135* (24), 9023−9031.
(29) DuBois, D. L.; Bullock, R. M. Molecular Electrocatalysts for the Oxidation of Hydrogen and the Production of Hydrogen - The Role of Pendant Amines as Proton Relays. *Eur. J. Inorg. Chem.* **2011**, *7*, 1017−1027.
(30) Horvath, S.; Fernandez, L. E.; Soudackov, A. V.; Hammes-Schiffer, S. Insights into proton-coupled electron transfer mechanisms of electrocatalytic H_2 oxidation and production. *Proc. Natl. Acad. Sci. U. S. A.* **2012**, *109* (39), 15663−15668.
(31) Zhang, L. H.; Mathew, S.; Hessels, J.; Reek, J. N. H.; Yu, F. S. Homogeneous Catalysts Based on First-Row Transition-Metals for Electrochemical Water Oxidation. *ChemSusChem* **2021**, *14* (1), 234−250.
(32) Joo, J.; Uchida, T.; Cuesta, A.; Koper, M. T. M.; Osawa, M. Importance of Acid-Base Equilibrium in Electrocatalytic Oxidation of Formic Acid on Platinum. *J. Am. Chem. Soc.* **2013**, *135* (27), 9991−9994.
(33) Kwon, Y.; Lai, S. C. S.; Rodriguez, P.; Koper, M. T. M. Electrocatalytic Oxidation of Alcohols on Gold in Alkaline Media: Base or Gold Catalysis? *J. Am. Chem. Soc.* **2011**, *133* (18), 6914−6917.
(34) Ma, J. J.; Wang, Z. M.; Majima, T.; Zhao, G. H. Role of Ni in PtNi Alloy for Modulating the Proton-Electron Transfer of Electrocatalytic Hydrogenation Revealed by the < i > In Situ</i> Raman-

https://doi.org/10.1021/jacs.3c06398
J. Am. Chem. Soc. XXXX, XXX, XXX−XXX

Rotating Disk Electrode Method. *ACS Catal.* **2022**, *12* (22), 14062−14071.
(35) Sun, Q.; Oliveira, N. J.; Kwon, S.; Tyukhtenko, S.; Guo, J. J.; Myrthil, N.; Lopez, S. A.; Kendrick, I.; Mukerjee, S.; Ma, L.; Ehrlich, S. N.; Li, J. K.; Goddard, W. A.; Yan, Y. S.; Jia, Q. Y. Understanding hydrogen electrocatalysis by probing the hydrogen-bond network of water at the electrified Pt-solution interface. *Nat. Energy* **2023**, *8* (8), 859−869.
(36) Li, P.; Jiang, Y. L.; Hu, Y. C.; Men, Y. N.; Liu, Y. W.; Cai, W. B.; Chen, S. L. Hydrogen bond network connectivity in the electric double layer dominates the kinetic pH effect in hydrogen electrocatalysis on Pt. *Nat. Catal.* **2022**, *5* (10), 900−911.
(37) Jackson, M. N.; Surendranath, Y. Molecular Control of Heterogeneous Electrocatalysis through Graphite Conjugation. *Acc. Chem. Res.* **2019**, *52* (12), 3432−3441.
(38) Warburton, R. E.; Hutchison, P.; Jackson, M. N.; Pegis, M. L.; Surendranath, Y.; Hammes-Schiffer, S. Interfacial Field-Driven Proton-Coupled Electron Transfer at Graphite-Conjugated Organic Acids. *J. Am. Chem. Soc.* **2020**, *142* (49), 20855−20864.
(39) Chen, X. T.; McCrum, I. T.; Schwarz, K. A.; Janik, M. J.; Koper, M. T. M. Co-adsorption of cations as the cause of the apparent pH dependence of hydrogen adsorption on a stepped platinum single-crystal electrode. *Angew. Chem., Int. Ed.* **2017**, *56* (47), 15025−15029.
(40) Ledezma-Yanez, I.; Wallace, W. D. Z.; Sebastian-Pascual, P.; Climent, V.; Feliu, J. M.; Koper, M. T. M. Interfacial water reorganization as a pH-dependent descriptor of the hydrogen evolution rate on platinum electrodes. *Nat. Energy* **2017**, *2* (4), 17031.
(41) Strmcnik, D.; Kodama, K.; van der Vliet, D.; Greeley, J.; Stamenkovic, V. R.; Markovic, N. M. The role of non-covalent interactions in electrocatalytic fuel-cell reactions on platinum. *Nat. Chem.* **2009**, *1* (6), 466−472.
(42) Haw, J. F.; Xu, T.; Nicholas, J. B.; Goguen, P. W. Solvent-assisted proton transfer in catalysis by zeolite solid acids. *Nature* **1997**, *389* (6653), 832−835.
(43) Merte, L. R.; Peng, G. W.; Bechstein, R.; Rieboldt, F.; Farberow, C. A.; Grabow, L. C.; Kudernatsch, W.; Wendt, S.; Lægsgaard, E.; Mavrikakis, M.; Besenbacher, F. Water-Mediated Proton Hopping on an Iron Oxide Surface. *Science* **2012**, *336* (6083), 889−893.
(44) Sato, R.; Ohkuma, S.; Shibuta, Y.; Shimojo, F.; Yamaguchi, S. Proton migration on hydrated surface of cubic ZrO_2: Ab initio molecular dynamics simulation. *J. Phys. Chem. C* **2015**, *119* (52), 28925−28933.
(45) Tocci, G.; Michaelides, A. Solvent-Induced Proton Hopping at a Water-Oxide Interface. *J. Phys. Chem. Lett.* **2014**, *5* (3), 474−480.
(46) Bertus, L. M.; Carcel, R. A. Prediction of TiO_2 and WO_3 nanopowders surface charge by the evaluation of point of zero charge (PZC). *Environ. Eng. Manag. J.* **2011**, *10* (8), 1021−1026.
(47) Cruywagen, J. J. Protonation, oligomerization, and condensation reactions of vanadate(V), molybdate(vi), and tungstate(vi). In *Advances in Inorganic Chemistry*; Sykes, A. G., Ed.; Academic Press, 1999; vol *49*, pp 127−182.
(48) Gulicovski, J. J.; Bračko, I.; Milonjić, S. K. Morphology and the isoelectric point of nanosized aqueous ceria sols. *Mater. Chem. Phys.* **2014**, *148* (3), 868−873.
(49) Mitchell, K. J.; Abboud, K. A.; Christou, G. Atomically-precise colloidal nanoparticles of cerium dioxide. *Nat. Commun.* **2017**, *8* (1), 1445.
(50) Regazzoni, A. E.; Blesa, M. A.; Maroto, A. J. G. Interfacial properties of zirconium dioxide and magnetite in water. *J. Colloid Interface Sci.* **1983**, *91* (2), 560−570.
(51) Durst, J.; Siebel, A.; Simon, C.; Hasché, F.; Herranz, J.; Gasteiger, H. A. New insights into the electrochemical hydrogen oxidation and evolution reaction mechanism. *Energy Environ. Sci.* **2014**, *7* (7), 2255−2260.
(52) Zheng, J.; Sheng, W. C.; Zhuang, Z. B.; Xu, B. J.; Yan, Y. S. Universal dependence of hydrogen oxidation and evolution reaction activity of platinum-group metals on pH and hydrogen binding energy. *Sci. Adv.* **2016**, *2* (3), No. 1501602.
(53) Zheng, J.; Zhou, S. Y.; Gu, S.; Xu, B. J.; Yan, Y. S. Size-Dependent Hydrogen Oxidation and Evolution Activities on Supported Palladium Nanoparticles in Acid and Base. *J. Electrochem. Soc.* **2016**, *163* (6), F499−F506.
(54) Sheng, W. C.; Zhuang, Z. B.; Gao, M. R.; Zheng, J.; Chen, J. G. G.; Yan, Y. S. Correlating hydrogen oxidation and evolution activity on platinum at different pH with measured hydrogen binding energy. *Nat. Commun.* **2015**, *6*, 5848.
(55) Chu, Y. Y.; Sanyal, U.; Li, X. H. S.; Qiu, Y.; Song, M. A.; Engelhard, M. H.; Davidson, S. D.; Koh, K.; Meyer, L. C.; Zheng, J.; Xie, X. H.; Li, D. S.; Liu, J.; Gutierrez, O. Y.; Wang, Y.; Shao, Y. Y. Tuning proton transfer and catalytic properties in triple junction nanostructured catalyts. *Nano Energy* **2021**, *86*, No. 106046.
(56) Koh, K.; Sanyal, U.; Lee, M. S.; Cheng, G. H.; Song, M.; Glezakou, V. A.; Liu, Y.; Li, D. S.; Rousseau, R.; Gutierrez, O. Y.; Karkamkar, A.; Derewinski, M.; Lercher, J. A. Electrochemically tunable proton-coupled electron transfer in Pd-catalyzed benzaldehyde hydrogenation. *Angew. Chem., Int. Ed.* **2020**, *59* (4), 1501−1505.
(57) Perdew, J. P.; Burke, K.; Ernzerhof, M. Generalized gradient approximation made simple. *Phys. Rev. Lett.* **1996**, *77* (18), 3865.
(58) Grimme, S.; Antony, J.; Ehrlich, S.; Krieg, H. A consistent and accurate ab initio parametrization of density functional dispersion correction (DFT-D) for the 94 elements H-Pu. *J. Chem. Phys.* **2010**, *132* (15), 154104.
(59) Kühne, T. D.; Iannuzzi, M.; Del Ben, M.; Rybkin, V. V.; Seewald, P.; Stein, F.; Laino, T.; Khaliullin, R. Z.; Schütt, O.; Schiffmann, F.; Golze, D.; Wilhelm, J.; Chulkov, S.; Bani-Hashemian, M. H.; Weber, V.; Borštnik, U.; Taillefumier, M.; Jakobovits, A. S.; Lazzaro, A.; Pabst, H.; Müller, T.; Schade, R.; Guidon, M.; Andermatt, S.; Holmberg, N.; Schenter, G. K.; Hehn, A.; Bussy, A.; Belleflamme, F.; Tabacchi, G.; Glöß, A.; Lass, M.; Bethune, I.; Mundy, C. J.; Plessl, C.; Watkins, M.; VandeVondele, J.; Krack, M.; Hutter, J. CP2K: An electronic structure and molecular dynamics software package - Quickstep: Efficient and accurate electronic structure calculations. *J. Chem. Phys.* **2020**, *152* (19), 194103 DOI: 10.1063/5.0007045.
(60) Goedecker, S.; Teter, M.; Hutter, J. Separable dual-space Gaussian pseudopotentials. *Phys. Rev. B* **1996**, *54* (3), 1703.
(61) Lippert, G.; Hutter, J.; Parrinello, M. A hybrid Gaussian and plane wave density functional scheme. *Mol. Phys.* **1997**, *92* (3), 477−488.

https://doi.org/10.1021/jacs.3c06398
J. Am. Chem. Soc. XXXX, XXX, XXX−XXX